



(This is a sample cover image for this issue. The actual cover is not yet available at this time.)

This article appeared in a journal published by Elsevier. The attached copy is furnished to the author for internal non-commercial research and education use, including for instruction at the authors institution and sharing with colleagues.

Other uses, including reproduction and distribution, or selling or licensing copies, or posting to personal, institutional or third party websites are prohibited.

In most cases authors are permitted to post their version of the article (e.g. in Word or Tex form) to their personal website or institutional repository. Authors requiring further information regarding Elsevier's archiving and manuscript policies are encouraged to visit:

<http://www.elsevier.com/copyright>



Contents lists available at ScienceDirect

International Journal of Impact Engineering

journal homepage: www.elsevier.com/locate/ijimpeng

Electro-magnetic collapse of thick-walled cylinders to investigate spontaneous shear localization

Z. Lovinger^{a,b,*}, A. Rikanati^b, Z. Rosenberg^b, D. Rittel^a^a Technion – Faculty of Mechanical Engineering, Technion, Haifa 32000, Israel^b RAFAEL, P.O. Box 2250, 21031, Israel

ARTICLE INFO

Article history:

Received 12 November 2010

Received in revised form

29 May 2011

Accepted 18 June 2011

Available online 26 June 2011

Keywords:

Thick-walled cylinder

Shear band

Electro-magnetic collapse

Numerical simulation

ABSTRACT

We present an electro-magnetic (EM) setup in order to collapse thick-walled cylinders, for the investigation of spontaneous formation of multiple adiabatic shear bands. The EM setup is based on a pulsed current generator using a capacitor bank system. The cylindrical specimen is part of an assembly of coaxial cylinders, where the inner and outer cylinders, each attached to an opposite pole, are short-circuited. Upon capacitor discharge, a high current flows through the cylinders, in opposite directions, creating repulsive magnetic forces between them. The outer cylinder is driven outwards and the inner cylinder is driven inwards – in a collapsing manner. This work presents the design procedure of the specimens' geometry using numerical simulations, and some preliminary experimental results for SS304L steel specimens. The spatial distribution of the multiple adiabatic shear bands in these specimens is in good agreement with that reported in the literature for explosively driven experiments with the same material. Our numerical simulations of the collapsing cylinder show good agreement with the experimental results for both global behavior and shear band distribution.

© 2011 Elsevier Ltd. All rights reserved.

1. Introduction

Shear localization is an important and often dominant failure mechanism at high strain rates, acting as a precursor to fracture and catastrophic failure. Issues related to the formation of adiabatic shear bands (ASB's) are: structural integrity and crashworthiness, product quality and efficiency in high speed machining and forming procedures, fragmentation, and several issues in the field of penetration mechanics as well as geophysical shear fault dynamics. In the development of armor and kinetic penetrators, for example, adiabatic shear banding plays a very important role. On the one hand ASB's are precursors to the plugging mechanism of strong targets, so that understanding and modeling the phenomenon are important for armor engineering. On the other hand, improved kinetic penetrators are designed with engineered materials which are susceptible to shear banding, resulting in the "self-sharpening" phenomenon, leading to enhanced penetration capabilities. Additional examples, which are characterized by the occurrence or multiple adiabatic shear bands are: (1) Collapsing of a cylindrical geometry, such as in the collapsing of a thick-walled cylinder; (2)

Fragmentation of cylindrical casings, which dominate the breakup dynamics, and (3) chip formation during cutting of high strength metals.

The formation of a shear band in a metal, undergoing large shear deformation, is related to a material instability. The strength of a material is controlled by two opposite mechanisms: the strain and strain-rate hardening mechanisms and the thermal softening mechanism. Under *static* loading, the main mechanism at work is strain hardening, which results in increasing strength with the progressing plastic deformation. Under *dynamic* loadings, other effects play an important role, mainly strain-rate hardening, pressure hardening and thermal softening. Under high rate deformation, thermal softening becomes a key element. Consequently, the classical approach explaining the initiation of adiabatic shear bands relates this phenomenon to a material instability, which takes place when the thermal softening overcomes the hardening mechanisms [1]. An alternative concept has been proposed, by Rittel et al. [2,3] who identified microstructural evolution (dynamic recrystallization) as the mechanism for shear band formation. These authors identified the dynamic stored energy of cold work as the driving force for ASB formation, which is preceded by dynamic recrystallization.

The idea of a material instability, under adiabatic loading, can be demonstrated in a schematic stress–strain curve as shown in Fig. 1. The negative slope of the adiabatic stress–strain curve, from the

* Corresponding author. Technion – Faculty of Mechanical Engineering, Technion, Haifa 32000, Israel. Tel.: +972 524290212.

E-mail address: cvloving@gmail.com (Z. Lovinger).

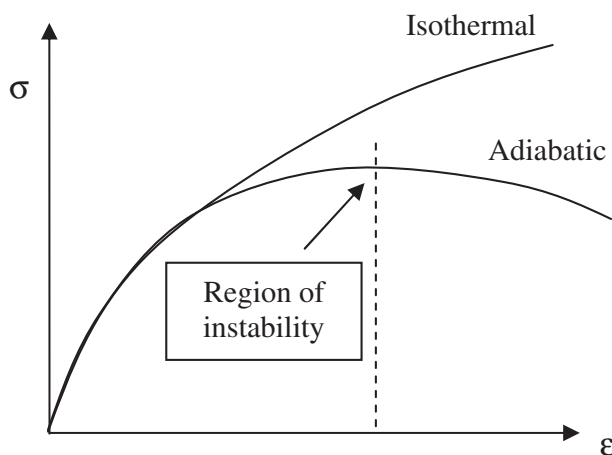


Fig. 1. Schematic isothermal and adiabatic stress–strain curves.

point of instability, results in a positive feedback for material softening, which is a key element in the evolution of an adiabatic shear band. This approach sets logical grounds for understanding the conditions for shear band evolution. However, the *initiation* of the shear band, with a prior stage of localization is a separate issue, influenced by different factors which should be further explained. In general, the initiation of shear banding is influenced by several factors:

- (1) Material thermo-mechanical properties;
- (2) Material microstructure;
- (3) Kinematic relations between the geometry of the specimen and its loading conditions.

Thermo-mechanical properties such as heat conductivity, strength, strain hardening, etc. are all believed to be related to the susceptibility of a material to adiabatic shear banding [4].

The influence of the microstructure is not conclusive and different results are drawn for different materials in the literature: a pronounced influence of the microstructure on shear band initiation was found for copper [5], yet no such influence was identified for stainless steel [6]. One can make use of intuitive reasoning and expect that microstructural defects and grain boundaries can determine the nucleation sites for the strain localization. Yet, the different results for the two materials indicate that additional material properties, coupled with the microstructure characteristics, play an important role, defining initiation sites of localization.

The third above-mentioned factor divides the ASB cases into two groups. The coupling between the specimen geometry and the nature of loading refers in general to two classes of shear band initiation (as referred to in the work on Chen et al. [17]):

- a. *Forced* shear localization
- b. *Spontaneous* shear localization

Forced shear localization – This is realized in plugging of plates, and high speed machining, dominated by direct shear forces. In these cases, shear bands will occur at regions where intense shear is defined by the boundaries of the loading instrument. One can generalize these cases by the definition that shear bands are formed in *well-defined regions*, parallel to the direction of the maximum shearing load.

Spontaneous shear localization – For these cases, the loading characteristics *do not* define the specific locations of directions for shear banding. *Multiple* shear bands can evolve in different regions

and in different directions which differ from the direction of the load. The advantage of examining spontaneous shear localization is that it highlights the *inherent susceptibility* of the material to adiabatic shear banding.

One of the most interesting load–geometry combinations, in which spontaneously-formed multiple adiabatic shear bands are observed, is the collapse of a thick-walled cylinder. In this case, an external pressure induces an inward collapse of the cylinder. The cylindrical symmetry defines no transverse boundary, and shear bands which evolve from the inner surface of the collapsing cylinder, do not form through a clear boundary or by stress concentration. Free of transverse boundary constraints, the initiation and propagation of the shear bands occur in a spontaneous manner.

Nesterenko et al. ([7,18]) introduced a controlled and repeatable way to create multiple shear bands in collapsing thick-walled cylinders. This technique is most suitable to study the properties and evolution of ASBs. The thick-walled cylinder (TWC) in this technique is sandwiched between two cylindrical copper shells. The shells are driven inwards by an explosive cylinder, while the outer and inner copper shells control the extent of collapse of the sample. The diagnostics are post-mortem: after the test, the sample is cut and polished to reveal the shear bands in the specimen.

Stokes et al. conducted several TWC experiments on the Pegasus-II facility using electro-magnetic forces as the driving collapsing force [19]. A distinct advantage was reported in these experiments with a more uniform collapse of the specimen, when compared to the explosively driven experiments which show some axial drive due to the directional ignition of the explosive driver. The use of electro-magnetic driving forces to collapse cylindrical specimens was presented also in the earlier work of Petit et al. [20]. They used a smaller EM facility (TROB-100 in the Kurchatov Institute) to drive collapsing cylinders in order to investigate the constitutive response of metals at high strain rates.

The use of explosives in these experiments or alternatively the use of a large scale MJ energy facility such as the Pegasus-II, makes this technique relatively complicated and expensive for performing a large series of experiments. The main motivation for the work presented here was to establish a simple experimental platform to perform large sets of experiments, enabling a detailed study on the evolution of multiple adiabatic shear bands.

In what follows we describe our experimental setup using electro-magnetic forces to collapse the thick-walled cylinders and discuss the process of designing the specimen's geometry, using 2D numerical simulations. We also conducted post-mortem analyses on SS304L specimens to reveal the spatial distribution of the adiabatic shear bands. In addition we carried out measurements of the current-flow and of the specimen's motion, in order to determine the conditions under which the specimen collapsed. We present typical experimental results of velocity histories and of the shear band distribution, and compare them with numerical simulations and experimental results obtained for the explosively driven TWC experiments, with the same material [6]. The shear band distribution is presented systematically for both experiments and simulations, using an empirical cumulative distribution function to apply a quantitative measure to compare the shear band distribution between experiments or between simulation and experiment.

2. Experimental setup

We use an electro-magnetic (EM) setup to provide the collapsing force on the cylindrical specimen. The EM setup is based on a pulsed current generator (PCG) using a 39 μ F capacitor bank system, shown in Fig. 2. The capacitors are charged with voltages of 20–30 kV which are released using an array of low inductance rail

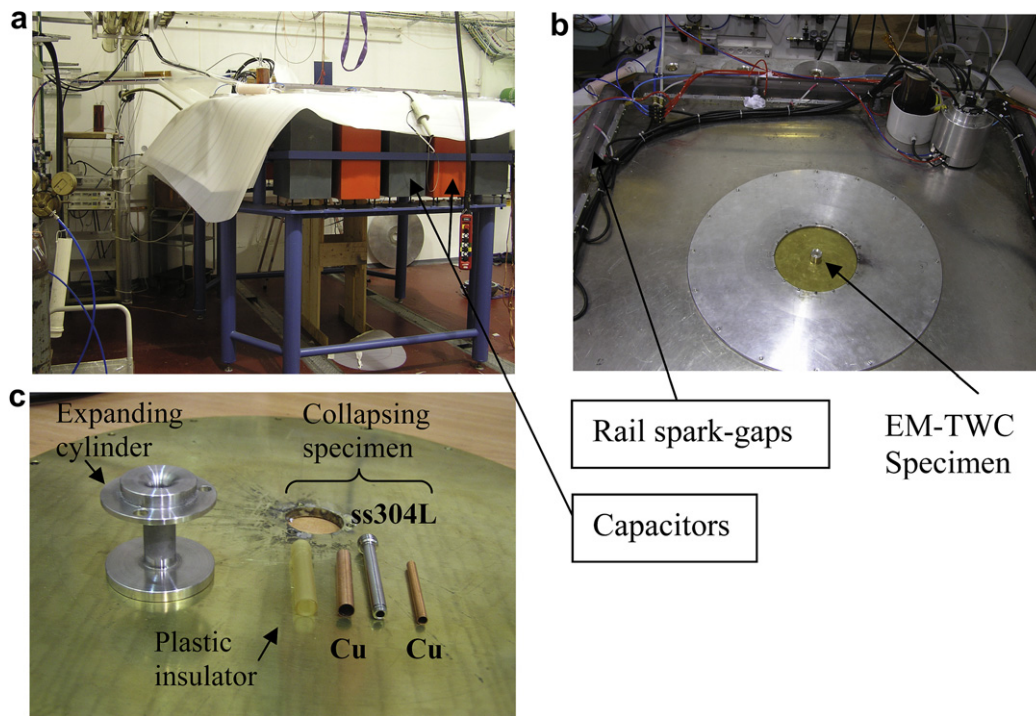


Fig. 2. The experimental setup: (a) general view and (b) top view of the pulsed current generator, (c) a typical specimen before assembly.

spark-gaps, allowing a fast discharge into the conductor system. The currents created are of the order of 1–2 MA, with a typical rise-time of $\sim 1 \mu\text{s}$. The conductor system is made of two plates, each attached to an opposite pole, separated by an isolating layer. The specimen is an assembly of coaxial cylinders, as shown in Figs. 2c and 3: an inner Cu cylinder, the tested specimen (SS, in this present study), an outer Cu cylinder (attached to the upper conductor plate), an insulating plastic cylinder and an outer SS cylinder (attached to the lower conductor plate). When the voltage is discharged, a current flows on both sides of the plastic insulator through the outer SS cylinder and the outer Cu cylinder, but in *opposite* directions, thus creating repulsive magnetic forces

between them. The outer cylinder is driven outwards and the inner cylinder is driven inwards – in a collapsing manner. The controllable parameters in the setup are the charging voltage of the capacitors, resulting in different magnetic pressures, and the specimen's geometry, controlling the extent of collapse and the stage of shear band evolution.

The main diagnostics is post-mortem: the collapsing cylinders, which come to a stop at the end of the experiment, are cut and polished to reveal the spatial distribution of shear bands and the spacing and lengths of the bands are measured. We also use in-situ diagnostics which provide more information about the specific conditions in each experiment. Specifically, we use a B-dot probe to assess the time history of the current-flow, and in some of the experiments we use a velocity interferometer to record the outgoing motion of the *expanding* outer cylinder. The B-dot measurement enables us to calculate the magnetic pressure acting on the specimen, while the sole purpose of the velocity measurement was to provide supplementary data to cross-check the calculated magnetic pressures.

3. Specimen design using numerical simulations

The first experiments were carried out with stainless steel SS304L specimens, as we had for it calibrated strength data and a shear-failure model which we could properly rely on for our simulations. Calibrated strength data and a shear-failure model for this material, are given in Ref. [8]. The calibration of the strength and failure models was done in two stages. First a flow–stress curve for the undamaged material was fitted to dynamic compression test data retrieved from split Hopkinson Pressure Bar (SHPB) tests, using the standard SHPB analysis. Then the two parameters of the shear-failure model (discussed in the sequel) were determined from a series of perforation tests detailed in Ref. [8]. In addition, results of TWC experiments with SS have been reported in the literature [6,10], allowing us to compare them with the results of our present experiments, conducted on a smaller scale. In Ref. [9],

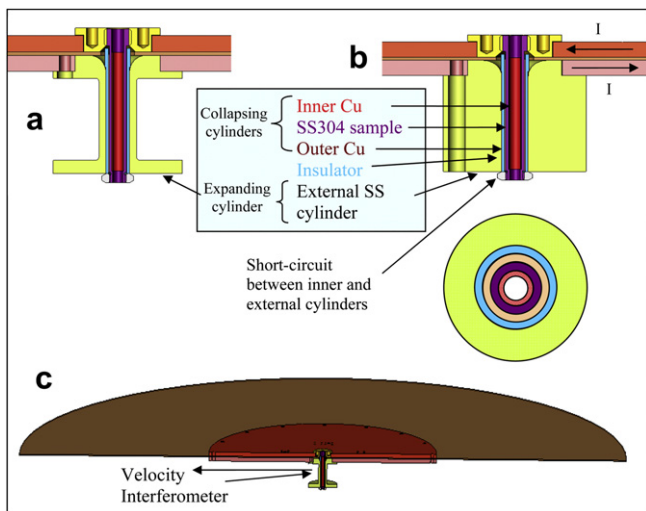


Fig. 3. Mechanical design of the experimental samples: (a) with a rigid external cylinder, (b) with a thin walled external cylinder for velocity interferometer measurements, (c) the assembly into the PCG system.

the ability of the calibrated models for SS to reproduce numerically multiple shear band evolution in thick-walled cylinders was demonstrated, comparing well with experimental data from explosively driven TWC experiments.

In order to design the TWC geometry, we first calculated the magnetic pressure and the typical diameter of the specimen, using the characteristic data of our PCG. The magnetic field B and the magnetic pressure P are given by:

$$B = \frac{\mu_0 I}{2\pi r}, P = \frac{\mu_0 I^2}{8\pi^2 r^2} \quad (1)$$

Where I is the current-flow, μ_0 is the permeability of free space, and r is the radius. In order to achieve magnetic pressures of 25–50 kbar, the typical diameter was determined to be 5 mm. The specimen thickness-to-radius ratio was adopted from the explosively driven TWC experiments [6], thus defining the initial geometry for the numerical simulations.

The simulations followed the inward motion of the specimen, making sure that it eventually stops and does not spall due to rarefaction waves.

3.1. Numerical model

We used an in-house 2D Lagrangian hydrocode which follows a finite difference explicit scheme. J_2 -plasticity is implemented in the scheme following Willkins' approach for the elastic–plastic flow, using the radial-return method to account for isotropic hardening [11]. Simulation results using this code were presented in previous work in Refs. [8] and [9].

The model uses slab symmetry (with plain strain conditions) and consists of three sandwiched cylinders Cu–SS–Cu. A boundary pressure, exerted on the external copper cylinder, is a half sin (in time), with a peak pressure of 25 kbar and duration of 2.0 μ s. The model configuration is shown in Fig. 4a.

For SS and Cu we use a Mie–Grüneisen Equation-of-state (EOS) referred to a $U = c + Su$ Hugoniot. The parameters for SS are: $\rho = 7.90$ g/cm³, $c = 4.57$ km/s, $S = 1.48$, $\Gamma = 1.75$. The parameters for Cu are: $\rho = 8.92$ g/cm³, $c = 3.93$ km/s, $S = 1.51$, $\Gamma = 1.98$. The shear

modulus is 71.5 GPa for SS and 44.0 GPa for Cu. For strength (of the undamaged material) we use the Johnson–Cook (JC) model [12]:

$$Y = (A + B\epsilon_p^n) \cdot \left(1 + C \ln \frac{\dot{\epsilon}_p}{\dot{\epsilon}_0}\right) \cdot \left(1 - \left(\frac{T - T_0}{T - T_m}\right)^m\right) \quad (2)$$

Where A , B , n , m and C are the material parameters, $\dot{\epsilon}_0$ is a reference strain rate, taken to be $\dot{\epsilon}_0 = 1$ sec^{−1}, T_0 is the initial temperature (room temperature in this case) and T_m the melting temperature. The parameters of the JC model we used in the simulations are: for SS304L: $A = 0.1$ GPa, $B = 1.072$ GPa, $C = 0.05$, $n = 0.34$. for OFHC copper: $A = 0.09$ GPa, $B = 0.292$ GPa, $C = 0.025$, $n = 0.31$, $m = 1.09$, $T_m = 1356$ °K. For SS304L, we use the JC model without the temperature term. Instead, we use a shear-failure model, which effectively corresponds to the thermal softening as detailed in Ref. [8]. The thermal softening, obtained using the temperature term of the JC model, is sufficient to correspond to the heating of the bulk material; however, in order to obtain localization of the ASB's, a more enhanced softening is essential – accomplished by the use of the shear-failure model. Briefly stated, we define a damage parameter $0 \leq D \leq 1$ which evolves by:

$$D = \frac{\epsilon - \epsilon_i}{\epsilon_f - \epsilon_i} \quad \epsilon_i < \epsilon < \epsilon_f \quad (3)$$

Where ϵ is the effective plastic strain and D is used to decrease the flow stress, Y , through:

$$Y = Y_0 \cdot (1 - D) = Y_0 \frac{\epsilon_f - \epsilon}{\epsilon_f - \epsilon_i} \quad (4)$$

Eq. (4) provides the positive feedback needed to cause shear localization. The model has two parameters: ϵ_i for which localization initiates, and ϵ_f for which the flow stress decreases to zero. The parameters for SS304L were calibrated by a series of perforation tests described in Ref. [8] and were found to be: $\epsilon_i = 0.30$, $\epsilon_f = 1.05$.

The initiation of localization is achieved in the simulation by numerical perturbations of the unstructured mesh we are using. The shear band distribution achieved in the simulations was found

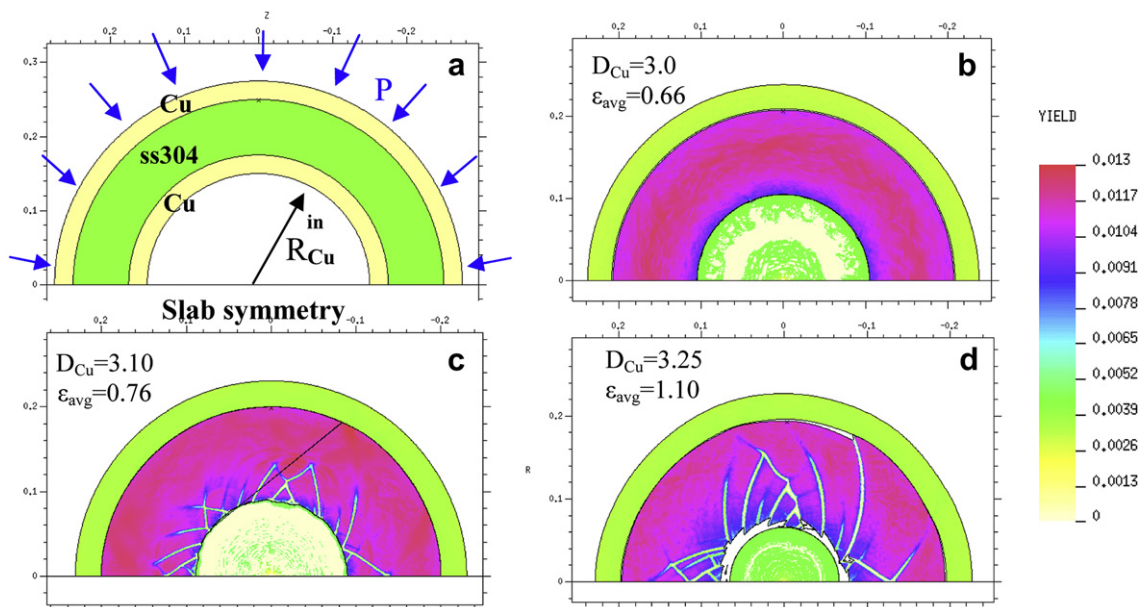


Fig. 4. Specimen design using numerical simulations: (a) model setup; Simulation results for the final stage of collapse: (b) with inner copper diameter = 3.0 mm, demonstrating the onset of shear bands, (c) with inner copper diameter = 3.10 mm, (d) with inner copper diameter = 3.25 mm.

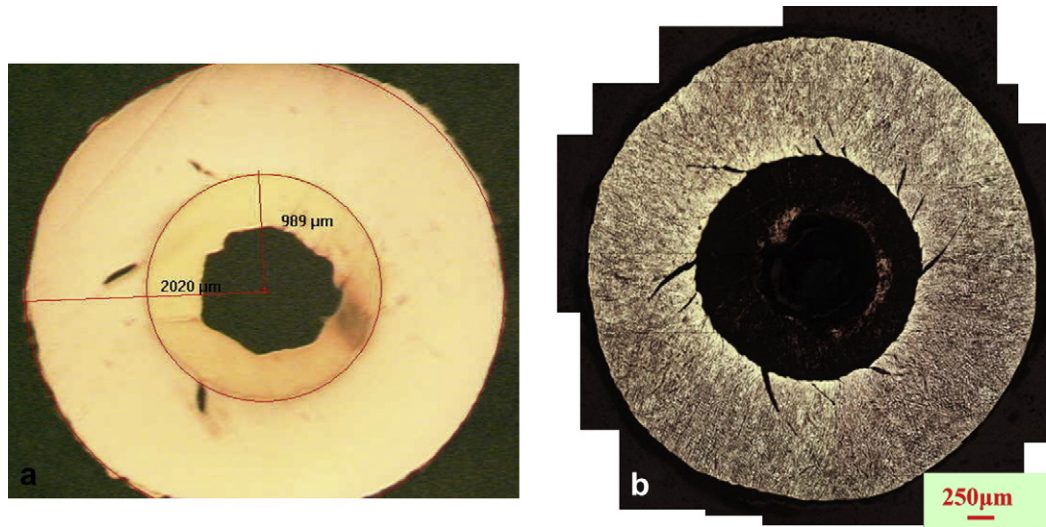


Fig. 5. Experimental results of specimen EM-TWC#1 collapsed to a final strain of 0.66: (a) before etching, (b) after etching.

to be insensitive to the characteristics of the initial numerical perturbation and this will be reported in a future paper. An alternative approach has been suggested in a recent work by Petit et al. [21], using a statistical distribution of mechanical properties as the initial perturbation for localization in such simulations.

3.2. Specimen design

Eventually, we defined from the simulations' results the following dimensions: the diameter of the outer copper cylinder is 5.0–5.5 mm, the diameter of the SS specimen is 3.5–5.0 mm and the outer diameter of the inner copper cylinder is 3.5 mm while its inner diameter changes for each of the three types of specimens, controlling the extent of collapse (final strain).

Fig. 4b–d shows the final stage of the three specimens, which were stopped at different stages of shear band evolution. The figures are flow stress maps on which the shear bands (with low or zero flow stress) are easily observed. Fig. 4b demonstrates an initial stage of shear band evolution for which a relatively homogeneous distribution of short shear bands exist. Fig. 4c and 4d shows further developed stages of shear band evolution corresponding to higher strains.

Additional considerations in the specimen design were:

1. The length of the cylinders: we aim to obtain an axi-symmetric collapse, free of longitudinal boundary interferences. We chose to examine two lengths of cylinders: $\sim \times 3$ and $\sim \times 6$ the typical diameter, namely, 15 mm and 30 mm long.
2. The dimensions of the *expanding* cylinder: the inductance of the system is affected by the relative displacements of the cylinders. Thus, larger displacement could cause shorter pulses, resulting in smaller forces to collapse the sample. Following this logic, the external cylinder was designed to be a thick and rigid one. Nevertheless, we designed also *thin*-walled external cylinders to enable the velocity interferometer measurements as explained above. The two specimen-types are shown in Fig. 3.

The resulting wall thickness of the SS304L collapsing cylinder is 0.75 mm. In order to probe the response of a polycrystal, we should require at least 10–15 grains through the thickness, meaning maximum grain sizes of 50–75 μm . The typical grain diameter for

the SS304L specimens was found to be $\sim 50 \mu\text{m}$, thus fulfilling this requirement.

4. Experimental results

We conducted a series of ten experiments with different geometries. All the samples collapsed and were successfully stopped. In each of the experiments the sample collapse was visually found to be very uniform lengthwise, for both the 15 mm and 30 mm long cylinders. Each specimen was sectioned perpendicularly to its axis, then polished and etched to examine the distribution of shear bands. We measured the dimensions of the collapsed cylinders with an optical microscope. These measurements determined the final effective strain which were reached at each experiment. Three of the experiments were conducted with velocity interferometer measurements, obtaining the velocity histories of the external cylinder's expansion.

Joule heating of the outer Cu cylinder caused melting of the external side of the cylinder, as was evident in each experiment. The current flows through the external Cu cylinder and the SS specimen is heated only by conduction from the external copper. As the overall time of collapse, calculated by simulations is about 8 μs , the SS specimen is not significantly heated over this short duration, having a negligible effect on the formation of the ASB's.

Figs. 5 and 6 show the experimental results of two specimens EM-TWC1 and EM-TWC2 cut at the middle section of the cylinders, polished and etched. The average plastic strain of the specimens, defined as:

$$\epsilon_p^{\text{eff}} = \frac{2}{\sqrt{3}} \left(\frac{r_f}{r_0} \right) \quad (5)$$

was calculated to be 0.66 and 0.76 respectively, where r_0 and r_f are the initial and final radii of the inner SS boundary.

The inner copper was recovered with a hole at its center, as seen in Figs. 5a and 6a. After measuring the collapsed dimensions and calculating the materials' volumes we found that the copper completed a full collapse into the center, and the observed hole in the center was created by a hot jet which formed when the copper collapsed on itself. Evidence of the copper jets was found also on a witness plate, placed perpendicular to the cylinders' axis. After etching, the specimens disclose an array of shear bands of different lengths. The best etching results for exposing the shear bands in the

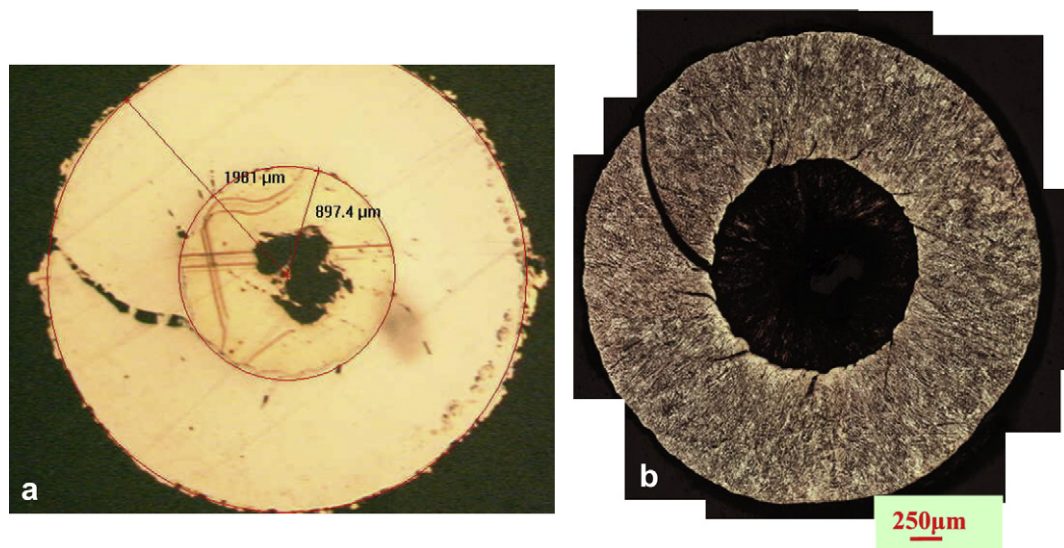


Fig. 6. Experimental results of specimen EM-TWC#2 collapsed to a final strain of 0.77:(a) before etching, (b) after etching.

specimens were achieved by using Kalling's No. 2 reagent [15]. For the spatial distribution of the shear bands we created a high-resolution picture and mapped the shear bands, yielding the distribution of band lengths as a function of the polar position. The shear band length distributions for the two specimens are presented in Fig. 7. A shielding effect is noticed in the specimens: areas adjacent to the well developed shear bands are characterized by smaller shear bands as they enter stress-relieved regions and their propagation is slowed down or arrested.

The shear band spacing at the inner boundary of the SS cylinder was evaluated for the different specimens. We determined the spacing at the initiation stage: evaluating the spacing between the shear bands sites for both small and well-developed shear bands. The spacing was found to be 100–150 μm for all specimens as shown in Fig. 8 and the average spacing in specimens #1 and #2 presented above was 120 μm and 129 μm respectively. This spacing was found to be in good agreement with the explosively driven TWC experiments with SS [6]. When addressing the question of what controls the spacing between initiated shear bands, two main approaches exist: one refers to the microstructure as controlling the initiation sites, such as grain boundaries, inclusions and impurities. The second approach, which consists of a perturbation analysis, predicts a characteristic wavelength, defining the shear band spacing at the initiation stage, e.g. [13,14]. The spacing by this approach is controlled by thermo-mechanical properties of the material and the relation between them, disregarding any influence of microstructure. In the work of Xue et al. [6] a systematic study of the influence of grain size in stainless steel on the shear band spacing in thick-walled cylinders showed similar spacing for a large range of grain sizes, even for grain sizes larger than the spacing between shear bands. The result shown here, demonstrating similar spacing for two different scales, gives additional support to their finding and to the prediction by perturbation analyses, indicating material thermo-mechanical properties as those controlling the spacing between shear bands.

4.1. Comparison with numerical simulations

We conducted 2D numerical simulations to examine the ability to reproduce the experimental results. We carried out two types of simulations:

- Simulations of the *collapsing* cylinders, comparing the final geometry and shear band distribution with those obtained in the experiment. As we have an error bar on the current-flow measurement, we determine, within the range defined by the error bar, the boundary pressure required to obtain the same final geometry of the collapsing sample.
- Simulations of the *expanding* SS304L cylinder, comparing the results with the velocity histories measured by the velocity interferometer. Again, we determine the boundary pressure required to match the velocity history of the expanding cylinder.

As shown above, we are conducting a simplified calculation in which the magnetic pressure is represented as an external boundary pressure. The shortcoming of this simplified approach compared to a full MHD calculation will be discussed in the sequel. Triantafyllidis, for example, discusses in Ref. [23] the limitations of calculating electro-magnetic forming problems with a magnetic boundary pressure in comparison to MHD calculations. A 10–15% difference in results is reported in Ref. [23] between the two approaches. This result points out that an equivalent boundary pressure could be a relatively good estimation which could be altered as an *equivalent* pressure, compensating some of the missing magneto-thermo-mechanical coupling.

4.1.1. Simulating the collapsing cylinders

We conducted numerical simulations of the experiments, taking into account the specific current-flow measured in each one. Typical histories of the current-flow and the magnetic pressure on the external boundary of the copper cylinder, as derived from the B-dot measurements, are shown in Fig. 9. Using the measured current-flow, we determined the magnetic pressure and its duration, which we then set as a boundary condition in our simulation. The measured current is 1.15 MA with an approximate error bar of $\pm 10\%$. Using Eq. (1), we obtain for the magnetic pressure a range of: $P_{\text{inner}} = 22.5\text{--}33.7$ kbar (note that the error for the pressure varies according to I^2). We examined different peak pressures within the calculated range and found a peak pressure of 25 kbar to agree best with the experimental results of the global behavior.

Fig. 10a shows a comparison between our simulations and the experimental results. The final geometry of the SS cylinder was: $D_{\text{out}} = 4.06$ mm, $D_{\text{in}} = 1.92$ mm, in our simulations and

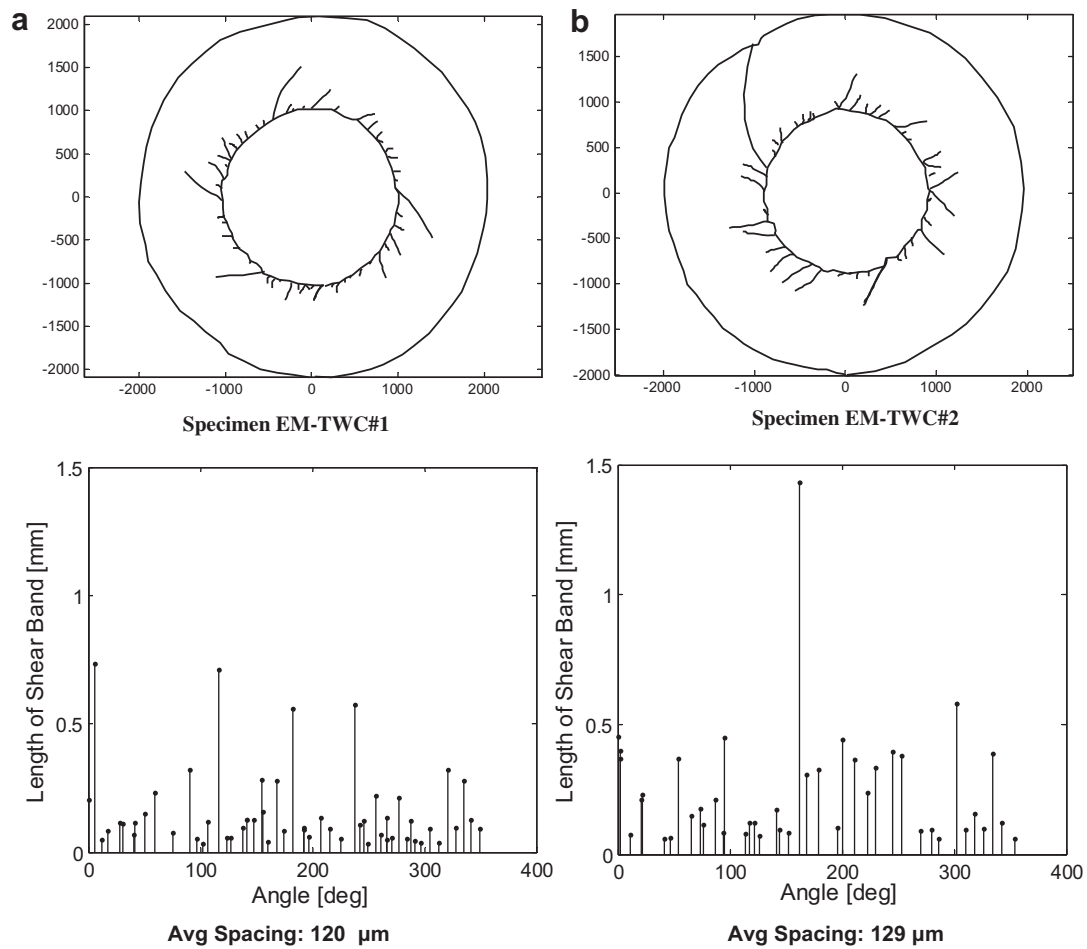


Fig. 7. Shear band length distribution in specimens (a) EM-TWC#1 and (b) EM-TWC#2.

$D_{out} = 4.04$ mm, $D_{in} = 1.96$ mm, measured on the specimen. To demonstrate the sensitivity of the simulation, Fig. 10b–d presents results for different boundary pressures with a peak of 20, 30 and 40 kbar. It can be seen that for the case of a 20 kbar peak pressure, no shear bands evolve, as the energy is too low and the specimen stops collapsing at an early stage prior to shear band initiation. By contrast, the 30 kbar peak pressure case shows a much more developed stage of shear band propagation and the external copper cylinder actually breaks apart. In the 40 kbar case, the energy left in the specimen after its convergence to the center, is much too high.

The outgoing shock wave, returning from the center, is strong enough to cause the specimen to spall and break. It can be seen from Fig. 10a that for a peak pressure of 25 kbar the shear band distribution compares well both in terms of spacing and lengths of the bands.

As a quantitative measure for comparing the shear band distribution between two experimental results as well as between experimental and simulation results, we use an empirical cumulative distribution function (ECDF). The ECDF does not follow a particular parametric form of a probability function but produces

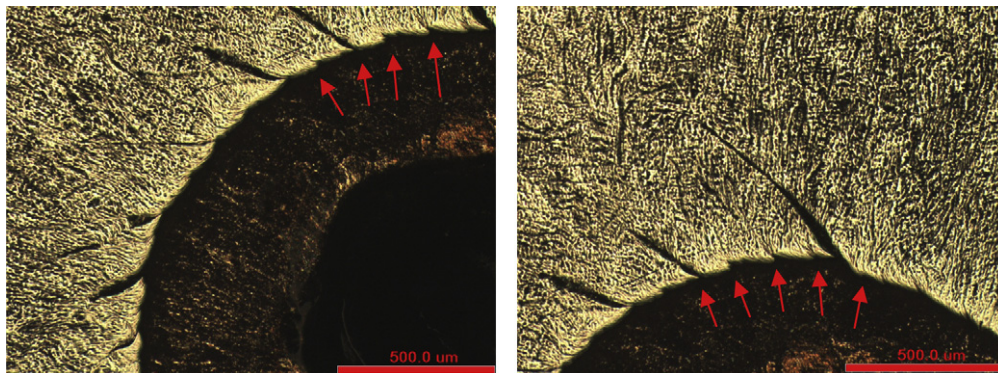


Fig. 8. Shear band spacing at the inner boundary of the SS specimen.

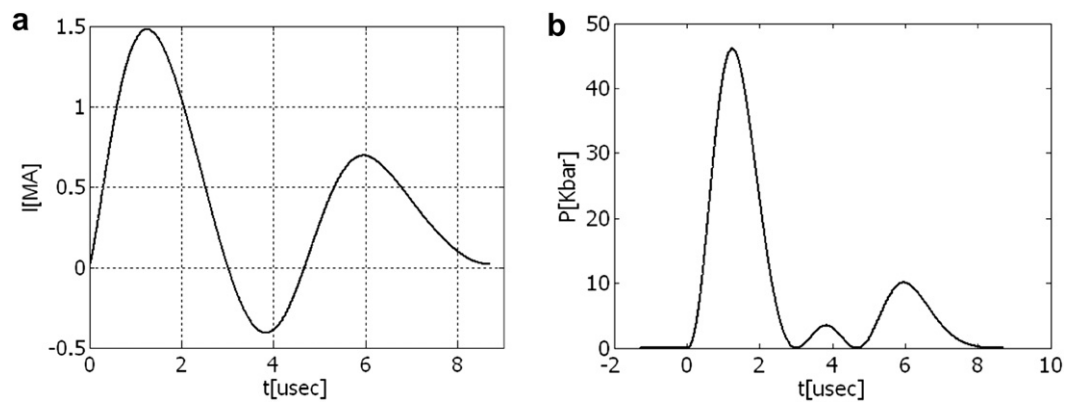


Fig. 9. Typical histories derived from the B-dot measurements (from exp#10): (a) measured current-flow history, (b) calculated boundary pressure on the external surface of the outer copper cylinder using Eq.(1).

a non-parametric density estimate that adapts itself to the data. The stair-step function simply assigns a probability of $1/n$ to each of the n observations in a sample. We use Greenwood's formula [16] for calculating lower and upper confidence bounds for the calculated ECDF.

Following this measure for comparison, the shear band distributions for both experiment and simulation are shown in Fig. 11, illustrating the shear band lengths as a function of the polar position. In addition, the ECDF for both cases are plotted together with the estimated upper and lower bounds of the experimental ECDF results.

The lengths of the well developed shear bands match quite well, and a shielding effect is noticed for both cases: areas adjacent to the well developed shear bands are characterized by smaller shear

bands as they enter stress-relieved regions. Also, the shear bands are more developed in the simulations which means that they are propagating at higher velocities. The ECDF measure demonstrates this, as the plotted cumulative function for the simulation results is lower for the entire span of lengths. The spacings in the two cases compare reasonably well: an average spacing of $95 \mu\text{m}$ is calculated for the simulation results, compared with an average spacing of $120 \mu\text{m}$ in the experiment. An additional difference between the simulations and the experimental results is observed in the directionality of shear bands. In the experiments, the shear bands follow mainly the $+45^\circ$ direction, whereas in the simulations an even directional distribution is observed in $\pm 45^\circ$. This directional tendency is not fully understood at this stage. Our assumption is that once a directional perturbation exists, the directionality will

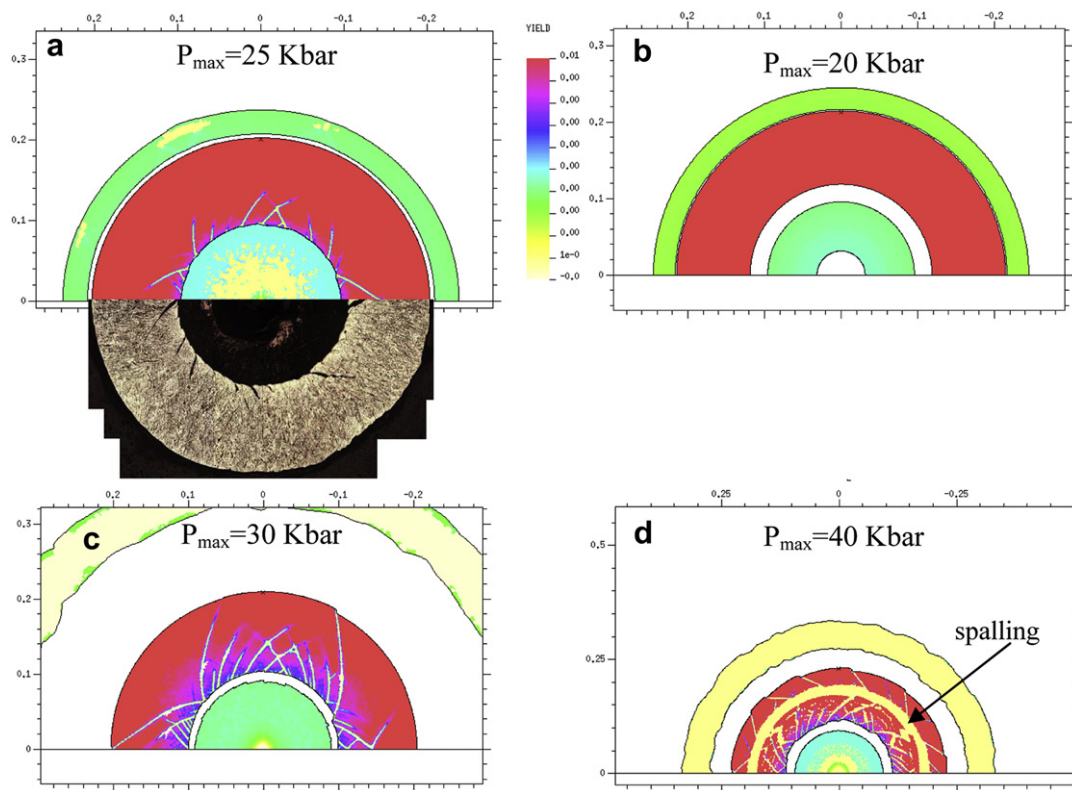


Fig. 10. Collapsing TWC simulations (yield maps) (a) with max pressure of 25 kbar, compared (lower picture) to the experimental result of specimen EM-TWC#1, (b) with max pressure of 20 kbar, (c) with max pressure of 30 kbar, (d) with max pressure of 40 kbar, resulting with spallation of the specimen.

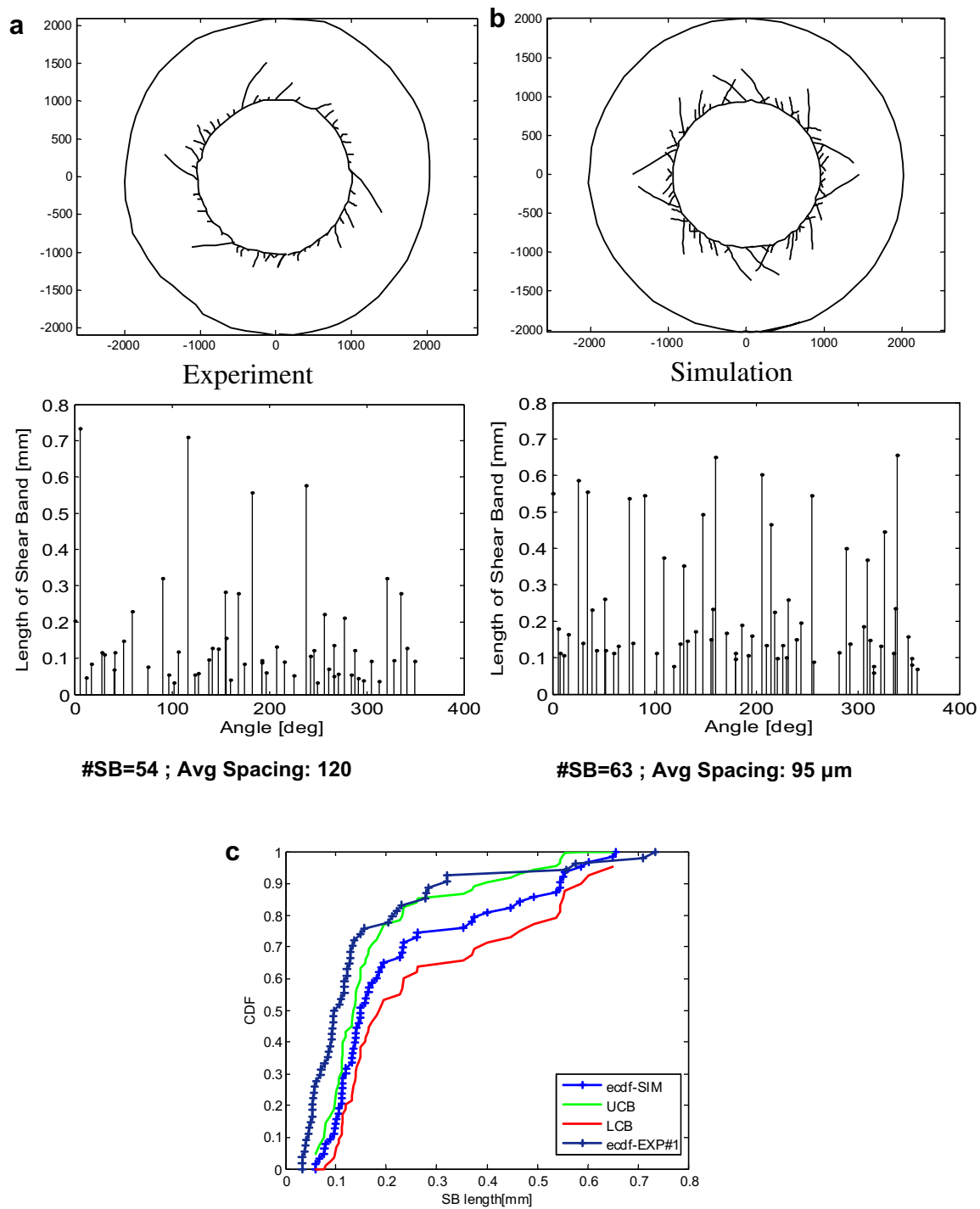


Fig. 11. Comparison of shear band length distribution for EM-TWC#1 (a) experiment Vs (b) simulation and (c) the empirical cumulative distribution function (ECDF) for simulation and experiment, plotted with upper ('UCB') and lower ('LCB') boundaries estimation.

build up due to the dynamics of the “shielding effect”, making it easier for adjacent shear bands to propagate in the same direction, rather than having the opposite 45° shear band propagate into the area relieved by release waves emanating from the sheared surfaces. Such a perturbation is not incorporated in the simulations. Yang et al. reported similar directionality in explosively driven TWC experiments conducted with Al7075 [22]. They showed in numerical simulations of the TWC experiments that adding heterogeneities into the model can cause such directionality of the shear bands. Using “soft” and “hard” particles in their model referring to

precipitated particles, inclusions or other imperfections which exist in the metallic alloy, they received a pronounced preferred direction of shear band evolution.

Finally, we demonstrate the mesh-size influence on our simulation results. Fig. 12 presents the simulation results for specimen EM-TWC#1 with the same boundary pressure (peak pressure of 25 kbar) using two cell sizes, 5 μm and 10 μm .

As the numerical scheme simulates a phenomenon initiated and dominated by an instability, the comparison between two numerical calculations, examining mesh-size effects in this case, will not

necessarily reproduce the *exact* pattern of shear bands with overlapping lines. Thus, a comparison between such simulations should relate to the shear band distribution, namely their spacing and lengths. We use here the ECDFs for both cases to demonstrate the state of convergence we are achieving.

It can be seen in Fig. 12 that the shear band distributions compare relatively well for the two cases. Some of the shear bands are identically observed while for some others, the development occurs symmetrically, namely the “matching” band develops at an angle -45° instead of $+45^\circ$, just as in the TWC experiments. It can also be noted that the number and maximum lengths of the shear bands are quite similar in both cases. However, when comparing the maximum length of the shorter shear bands, namely those which come to a stop at an earlier stage of evolution, the two distributions differ. In fact, the lower resolution calculation predicts longer short shear bands than the higher resolution ones. This is also apparent in the ECDF plots, in Fig. 12, as the CDF matches well between the two cases for the longer shear bands and differs at the lower part of the plot, for the short shear bands. This result indicates that for the finer resolution, the shear band velocities remain quite the same as for the coarser resolution, yet the shielding effect

is more enhanced, creating the initiated shear bands to come to a stop at shorter lengths.

4.1.2. Simulating the expanding cylinders

The measured velocity in experiment EM-TWC6 is shown in Fig. 13. We used two Velocity Interferometers to examine the axial symmetry of the expanding motion. Both signals seem to overlap, reaching a peak velocity of about 55 m/s with duration of $\sim 6 \mu\text{s}$. It could be seen from the experimental signal that the rise and the fall-time are not symmetric: As the rise-time is about $1 \mu\text{s}$, while the fall-time is significantly larger, about $5 \mu\text{s}$.

As for the case of the collapsing cylinder, we calculated the magnetic pressure acting on the external SS cylinder, this time using in Eq. (1) the inner radius of the external SS cylinder, where the current is assumed to flow. Accounting again for the $\pm 10\%$ error in the current-flow measurements, we obtain for the magnetic pressure a range of: $P_{\text{inner}} = 13.9\text{--}20.8 \text{ kbar}$.

We conducted simulations of the external SS cylinder, following the same simplified approach using a boundary pressure – this time with an internal boundary pressure, as shown in Fig. 13. The simulations were conducted with different peak pressures,

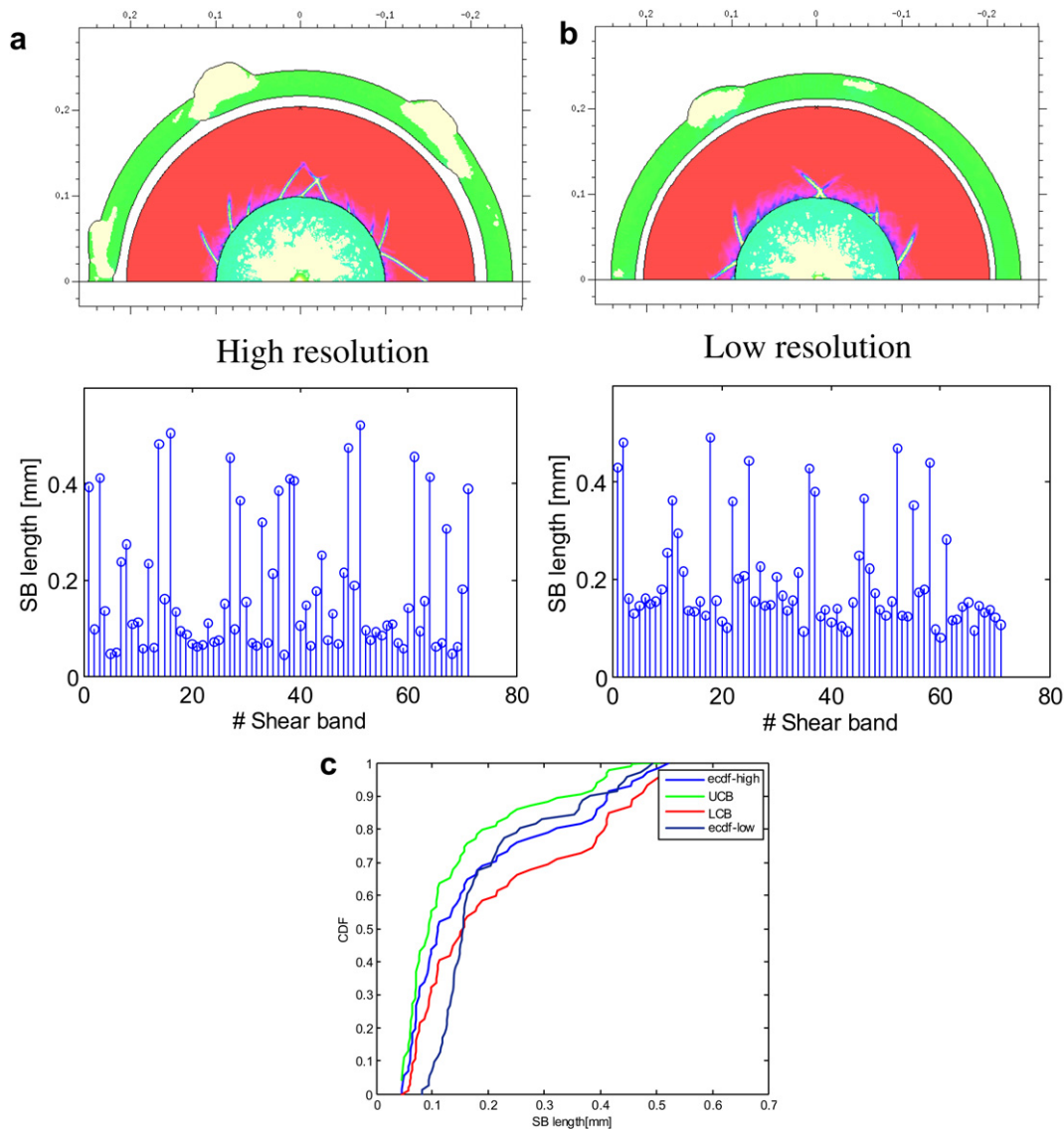


Fig. 12. TWC simulations: yield maps and shear band distribution of EM-TWC#1 – with two resolutions: (a) High resolution – with cell size of $5 \mu\text{m}$ and (b) Low resolution – with cell size of $10 \mu\text{m}$, (c) ECDF for the two resolutions, with upper and lower bounds of the high-resolution CDF.

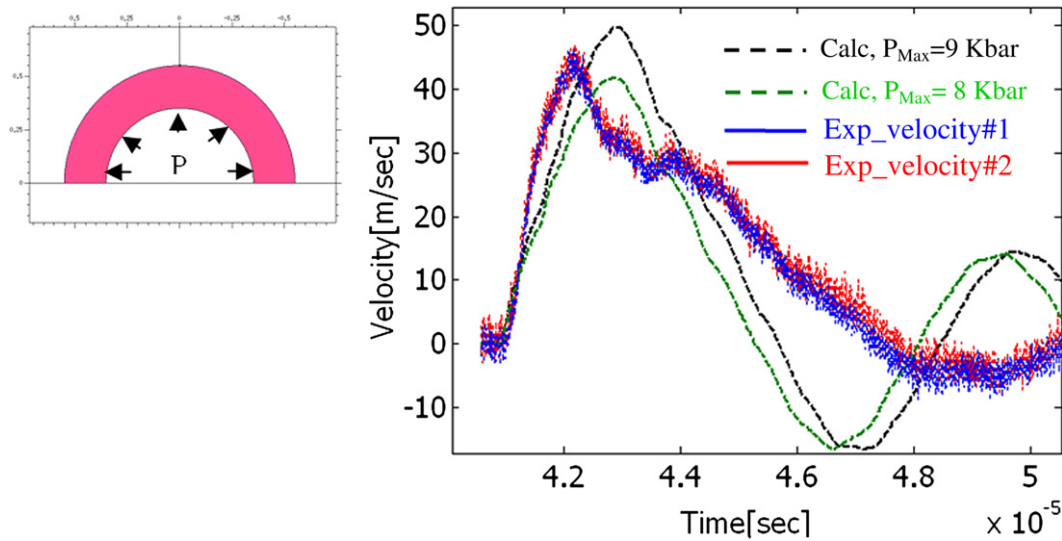


Fig. 13. Expanding cylinder simulations: velocity histories of the external boundary of the SS cylinder: measured and simulated signals.

comparing the external boundary velocity with the interferometer measurements. A reasonable agreement is obtained between the measured and calculated free surface velocities if we assume that $P_{\text{inner}} = 9.0$ kbar, which is clearly inferior to the above-mentioned theoretically estimated values. Furthermore, the simulation does not reproduce the shape of the signal, having a steeper descend than obtained in the experiments. This observation calls for future examination of possible skin depth or thermal effects which might explain the missing physics that are currently omitted in the simplified assumptions of a simple pressure boundary condition. A short discussion of these effects follows.

4.1.2.1. Skin depth effects. As explained above, we are using a boundary pressure condition to account for the magnetic pressure developed in the experiment. In practice, the current is flowing within a finite depth, defined as the skin depth. The skin depth is a function of the electrical conductivity of the material (σ_0) and of the current frequency (ω) and is defined as:

$$\delta = \sqrt{\frac{2\kappa_0}{\omega}}, \quad \omega = \frac{2\pi}{T}, \quad \kappa_0 = \frac{1}{\sigma_0\mu} \quad (6)$$

where κ_0 is the magnetic diffusivity and μ is the permeability.

The skin depth, calculated with the typical duration of $T = 2.0$ μs , is found to be:

For Cu : $\delta = 92$ μm –0.1 mm;
For SS: $\delta = 354$ μm –0.35 mm.

The skin depth for SS is much larger due to its lower conductivity. The meaning of a large skin depth (such as in the SS) is that the magnetic pressure is distributed within the skin depth area, significantly different than a boundary pressure-load, as used in our simulations. Hence, the boundary pressure in our simulations is in practice an effective pressure which must be smaller and distributed within the skin depth, to represent the actual conditions. As the skin effect is smaller, the difference between the effective boundary load and the actual distribution becomes smaller. Therefore, for copper, a small skin effect is expected, while for SS its effect should be significant. In order to examine this issue, we simulated the skin effect by distributing the calculated pressure exponentially through the skin depth, partly as body-forces.

Nevertheless, this had no significant change on the simulated interferometer signal. We intend to examine this issue experimentally by changing the expanding cylinder's material to a material with a small skin depth, such as copper.

4.1.2.2. Thermal effects. The current, flowing through limited layers on the external boundary of the outer copper cylinder and on the inner boundary of the external steel cylinder, causes extensive heating to high temperatures within these layers. The joule heating of the copper was discussed above, referring to the collapsing cylinder. Yet, the rapid heating of these layers might influence also the motion of the external cylinder. Referring to the thermal effects, we can propose two explanations to address the asymmetric oscillation of the interferometer's signal:

1. A change in the rigidity of the expanding cylinder: the high temperatures, evolving within the skin depth, soften the material in this layer, degrading the rigidity of the cylinder and resulting with a lower frequency vibration.
2. An additional load evolving from the inner boundary: this might be a result of additional pressure caused by ablation of the external boundary of the copper cylinder due to the very high temperature it reaches.

These assumptions will be further examined in simulations, in future work, to enable better understanding of this behavior and enable better comparison with the interferometer's signals.

All in all, it should be noted that, while the reconstruction of the interferometer's signals is important for a better understanding of the coupled physics involved in the EM system, it has no real significance to the actual shear banding phenomena investigated in the collapsed cylinder, as the latter is ultimately influenced by the final strain reached.

5. Summary and conclusions

We developed an experimental technique for the collapse of thick-walled cylinders using electro-magnetic forces. This technique enables one to conduct large sets of experiments in order to explore the spontaneous evolution of multiple adiabatic shear bands in thick-walled cylinders. The measured spacing between

shear bands show good agreement with that obtained in the explosively driven, larger scaled experiments using the same material. This result, demonstrating similar spacing for two different scales, supports the prediction by perturbation analyses of a characteristic wavelength which defines the shear band spacing at the initiation stage. We conducted 2D numerical simulations for both the collapsing cylinder and the expanding one and compared our results with the experimental measurements. The shear band distribution is presented systematically for both experiments and simulations, using an empirical cumulative distribution function to apply a quantitative measure to compare the shear band distribution between experiments or between simulation and experiment. Our simulations of the collapsing cylinder show good agreement with the experimental results for both global behavior and shear band distribution. In future work, we intend to use this new experimental technique, on different materials. This will result in better understanding of the initiation and evolution of spontaneous shear bands in this complex loading-geometry, in order to establish better modeling abilities of the phenomenon.

Acknowledgments

We would like to acknowledge the work and assistance of Uri Avni and Eli Yeger conducting the experiments and the work of Shalom Aricha designing the specimens.

References

- [1] Zener C, Hollomon JH. Effect of strain rate upon plastic flow of steel. *J Appl Phys*; 1943;22–32.
- [2] Rittel D, Landau P, Venkert A. Dynamic recrystallization as a potential cause for adiabatic shear failure. *Phys Rev Lett* 2008;101.
- [3] Rittel D, Wang ZG, Merzer M. Adiabatic shear failure and dynamic stored energy of cold work. *Phys Rev Lett* 2006;96.
- [4] Bai Y, Dodd B. Adiabatic shear localization: occurrence, theories and applications. Pergamon Press; 1992.
- [5] Bondar MP, Merzhievskii LA. Evolution of the metal microstructure and conditions of strain localization under high-strain-rate loading. *Comb Expl Shock Waves* 2006;42(3):356–65.
- [6] Xue Q, Meyers MA, F Nesterenko V. Self organization of shear bands in steel. *Mat Sci Eng A* 2004;384:35–46.
- [7] Nesterenko VF, Bondar MP. Localization of deformation in collapse of a thick walled cylinder. *Comb Expl Shock Waves* 1994;30(4):500–5.
- [8] Firstenberg O, Ashuach Y, Partom Y. A simple model for dynamic shear failure of stainless steel, 8th Int. Conference on mechanical and physical behavior of materials under dynamic loading. *J Phys IV France* 2006;134:191–6.
- [9] Lovinger Z, Partom Y. Simulation of multiple shear bands in collapsing cylinder experiments, 8th Int. Conference on mechanical and physical behaviour of materials under dynamic loading. *DYMAT*; 2009:1649–56.
- [10] Meyers MA, Xu YB, Xue Q, Perez-Prado MT, R McNelly T. Microstructural evolution in adiabatic shear localization in stainless steel. *Acta Materialia* 2003;51:1307–25.
- [11] Wilkins ML. Calculation of elastic-plastic flow. In: Alder B, Fernbach S, Rotenberg M, editors. *Methods in computational physics*, vol. 3. New York: Academic Press; 1964. p. 211–63.
- [12] Johnson GR, Cook WH. A constitutive model and data for metals subjected to large strains, high strain rates and high temperatures, *Proceedings of 7th International Symposium on Ballistics*, The Hague, The Netherlands, 1983. pp. 541–547.
- [13] Wright TW, Okendon H. A scaling law for the effect of inertia on the formation of adiabatic shear bands. *Int J Plasticity* 1996;12(7):927–34.
- [14] Molinari A. Collective behavior and spacing of adiabatic shear bands. *J Mech Phys Solids* 1997;45(9):1551–75.
- [15] ASM Metals Handbook. In: *Metallography and microstructures*. 9th ed., vol 9. USA: ASM International; 1985.
- [16] Cox DR, Oakes D. *Analysis of survival data*. London: Chapman & Hall; 1984.
- [17] Chen YJ, Meyers MA, F Nesterenko V. Spontaneous and forced shear localization in high strain-rate deformation of tantalum. *Mat Sci Eng A* 1999;286:70–82.
- [18] Nesterenko VF, Lazaridi AN, Pershin SA. Localization of deformation in copper by explosive compression of hollow cylinders. *Fizika Goreniya i Vzryva* 1989;25(4):154–5 (in Russian).
- [19] Stokes JL, Nesterenko VF, Shlachter JS, Fulton RD, Indrakanti SS, Gu Ya Bei. Comparative behavior of Ti and stainless steel in a magnetically-driven implosion at the Pegasus-II facility. In: Staudhammer KP, Murr LE, Meyers MA, editors. *Proceedings of international conference on fundamental issues and applications of shock-wave and high-strain-rate phenomena*. Amsterdam: Elsevier; 2001. p. 585–92.
- [20] Petit J, Alexeev YA, Ananiev SP, Kazeev MN. The electro-magnetic cylindrical compression: a tool to test behavior modeling under large strain at high strain rate. *J Phys IV France* 1997;7.
- [21] Petit J. An approach to generate random localizations in Lagrangian numerical simulations. Chapter 14. In: Buzaud E, Ionescu R, Voyiadjis GZ, editors. *Materials under extreme loadings-application to penetration and impact*. ISTE and Wiley; 2010.
- [22] Yang Y, Li DH, Zheng HG, Li XM, Jiang F. Self organization behaviors of shear bands in 7075T73 and annealed aluminum alloy. *Mat Sci Eng* 2009;A527:344–54.
- [23] Triantafyllidis N, Waldenmyer JR. Onset of necking in electro-magnetically formed rings. *J Mech Phys Solids* 2004;52:2127–48.